


Joint *Suzaku* and *Chandra* observations of the MKW4 galaxy group out to the virial radius

Arnab Sarkar,¹  Yuanyuan Su,¹  Scott Randall,²  Fabio Gastaldello,³  Isabella Trierweiler,⁴
Raymond White,⁵ Ralph Kraft,²  Eric Miller⁶ 

¹*Physics and Astronomy, University of Kentucky, 505 Rose street, Lexington, KY 40506, USA*

²*Harvard-Smithsonian Center for Astrophysics, 60 Garden Street, Cambridge, MA 02138, USA*

³*Instituto di Astrofisica Spaziale e Fisica Cosmica (INAF-IASF), Milano, via A. Corti 12, I-20133 Milano, Italy*

⁴*Division of Astronomy and Astrophysics, University of California Los Angeles, Los Angeles, CA*

⁵*Department of Physics and Astronomy, University of Alabama, Box 870324, Tuscaloosa, AL 35487, USA*

⁶*Kavli Institute for Astrophysics & Space Research, Massachusetts Institute of Technology, 77 Massachusetts Ave, Cambridge, MA 02139, USA*

Accepted for publication in MNRAS

Accepted 2020 December 8. Received 2020 December 7; in original form 2020 November 4

ABSTRACT

We present joint *Suzaku* and *Chandra* observations of MKW4. With a global temperature of 1.6 keV, MKW4 is one of the smallest galaxy groups that have been mapped in X-rays out to the virial radius. We measure its gas properties from its center to the virial radius in the north, east, and northeast directions. Its entropy profile follows a power-law of $\propto r^{-1.1}$ between R_{500} and R_{200} in all directions, as expected from the purely gravitational structure formation model. The well-behaved entropy profiles at the outskirts of MKW4 disfavor the presence of gas clumping or thermal non-equilibrium between ions and electrons in this system. We measure an enclosed baryon fraction of 11% at R_{200} , remarkably smaller than the cosmic baryon fraction of 15%. We note that the enclosed gas fractions at R_{200} are systematically smaller for groups than for clusters from existing studies in the literature. The low baryon fraction of galaxy groups, such as MKW4, suggests that their shallower gravitational potential well may make them more vulnerable to baryon losses due to AGN feedback or galactic winds. We find that the azimuthal scatter of various gas properties at the outskirts of MKW4 is significantly lower than in other systems, suggesting that MKW4 is a spherically symmetric and highly relaxed system.

Key words: X-rays: galaxies: clusters – galaxies: clusters: intracluster medium

1 INTRODUCTION

A significant fraction of all the baryons of the Universe, including more than half of the galaxies, reside in groups and low mass clusters (e.g., Eke et al. 2004; Springel & Hernquist 2003). In the standard CDM structure formation model, clusters continue to grow and evolve through mergers and accretions, largely along cosmic filaments, in their outer regions (Walker et al. 2019). These processes may leave distinctive marks in the gas properties at cluster outskirts, including inhomogeneous gas density distributions, turbulent gas motions, and electrons that are not in thermodynamic equilibrium with the ions in the intra-cluster medium (ICM). Groups are expected to be more evolved than massive clusters, as their sound crossing times are short compared to the Hubble time (0.1–0.5 H_0^{-1} , Paul et al. 2017). However, due to their shallower gravitational potential wells, groups are more sensitive to non-gravitational processes, such as galactic winds, star formation, and feedback from active galactic nuclei (AGN, e.g., Lovisari et al. 2015; Pratt et al. 2010; Mathews & Guo 2011; Humphrey et al. 2012; Thölken et al. 2016). Probing the

gas properties of galaxy groups out to their virial radii thus provides a powerful approach to investigating their growth and evolution.

In galaxy cluster studies, entropy, as a function of radius, records the thermal history of the ICM (e.g., Borgani et al. 2005; McCarthy et al. 2010). Entropy is empirically defined as $K(r) = T/n_e^{2/3}$, where n_e and T are the electron density and gas temperature, respectively. A growing number of X-ray observations have been made for cluster outskirts (e.g., Simionescu et al. 2017; Ghirardini et al. 2018). The majority of these works study the properties of massive galaxy clusters ($T_X > 3$ keV), while there is a lack of detailed studies of the outskirts of galaxy groups. The studies of massive clusters have brought up unexpected results (e.g., Urban et al. 2014a; Simionescu et al. 2017; Ghirardini et al. 2018) such as the flattening or even a drop of entropy profiles between R_{500}^\dagger and R_{200} relative to the expectation from numerical simulations of the gravitational collapse model (Voit et al. 2005). Several explanations have been proposed to explain the deviation of entropy profiles from the self-similar value, e.g., the breakdown of thermal equilibrium between electrons and

* E-mail: arnab.sarkar@uky.edu

$^\dagger r_\Delta$ = radius from cluster core where matter density is Δ times the critical density of the Universe.

protons (Akamatsu et al. 2011) or inhomogeneous gas density distribution (gas clumping) at cluster outskirts (Nagai & Lau 2011). Accretion shocks at the cluster outskirts tend to heat the heavier ions faster than electrons, causing thermal non-equilibrium between electrons and ions and leading to a lower gas entropy (e.g., Akamatsu et al. 2011; Hoshino et al. 2010). Unresolved cool gas clumps were invoked by Simionescu et al. (2011) and Nagai & Lau (2011) to explain the observed entropy flattening, since the denser, cooler clumps have a higher emissivity than the local ICM. The clumping factor is defined as

$$C = \frac{\langle n_e^2 \rangle}{\langle n_e \rangle^2}, \quad (1)$$

where n_e is the electron density. Simionescu et al. (2011) estimate a clumping factor of $C \approx 16$ for the Perseus cluster. Bonamente et al. (2013) and Walker et al. (2012a) report $C \approx 7$ for Abell 1835 and $C \approx 9$ for PKS 0745-191, respectively. In contrast, a handful of observations have indicated that low mass clusters ($T_X < 3$ keV) show little to no flattening in their entropy profiles (e.g., RXJ1159, Su et al. 2015; A1750, Bulbul et al. 2016; UGC 03957, Thölken et al. 2016), presumably because groups have lower clumping factors at their outskirts. Galaxy groups may provide essential constraints on whether their entropy profiles behave in a self-similar way compared to galaxy clusters.

MKW4 is a cool core cluster at $z \sim 0.02$ with a global temperature of 1.6 keV (Sun et al. 2009). It contains nearly 50 member galaxies, including NGC 4073, the brightest group galaxy (BGG). The NGC 4073 is about 1.5 times brighter than the second-brightest galaxy in the group (O’Sullivan et al. 2003). Unlike massive clusters, the outskirts of galaxy groups are relatively unexplored due to their low surface brightness. The typical ICM surface brightness in group outskirts falls below 20% of the total emission. The measurement of their gas properties is therefore extremely challenging. The now-defunct *Suzaku* X-ray telescope with its low particle background helped unravel this new frontier. However, *Suzaku* can only resolve point sources down to a flux level of 10^{-13} erg cm $^{-2}$ s $^{-1}$ due to its modest PSF ($\sim 3'$), which causes significant statistical and systematic uncertainties in the measurement of gas properties at the group outskirts. Thanks to the superb angular resolution of *Chandra*, even with the modest exposures it increases the number of detected point sources by 1 dex, which allows tighter constraints on the cosmic X-ray background (CXB) uncertainties (Miller et al. 2012).

We utilize deep *Suzaku* and snapshot *Chandra* observations to probe the thermal properties of MKW4 out to its virial radius in multiple directions, which we present in this paper. The metallicity distribution of MKW4 will be presented in a following paper. Using NASA/IPAC Extragalactic Database,[‡] we calculate a luminosity distance of 83 Mpc ($1'' = 0.443$ kpc) for $z = 0.02$, adopting a cosmology of $H_0 = 70$ km s $^{-1}$ Mpc $^{-1}$, $\Omega_\Lambda = 0.7$, and $\Omega_m = 0.3$. All reported uncertainties in this paper are at 1σ confidence level unless mentioned otherwise.

2 OBSERVATIONS AND DATA REDUCTION

MKW4 has been mapped with 6 *Suzaku* pointings from its center out to the virial radii in the north, east, and north-east directions, as

shown in Figure 1. It has also been observed with a deep *Chandra* ACIS-S observation at its center and three snapshot *Chandra* ACIS-I observations overlapping with the three outer *Suzaku* pointings in three directions. Below we describe the data reduction processes and spectral fitting for each of the observations.

2.1 Suzaku

MKW4 has been mapped with three X-ray Imaging Spectrometer (XIS) instruments onboard *Suzaku* – two front-illuminated CCDs (XIS0, XIS3), and one back-illuminated CCD (XIS1). The observation logs are summarized in Table 1. All three XIS instruments were in the normal clocking mode without window and burst options during the observations.

2.1.1 Data reduction

The *Suzaku* data was reduced using HEASoft 6.25, CIAO 4.11, and the XIS calibration database (CALDB) version 20181010. We followed a standard data reduction thread[§] to process all the event files. The 5×5 mode event files were converted to the 3×3 mode event files and combined with the other 3×3 mode event files. The resulting event files were filtered for calibration source regions and bad pixels with *cleansis*. We selected events with GRADE 0, 2, 3, 4, and 6. Light curves were filtered for flares using the *lc_clean* task of CIAO 4.11. The resolved point sources were identified visually. We did not exclude those sources while extracting spectra, because exclusion would result in a very low photon count available for the spectral analysis. We instead took the advantage of *Chandra* observations to estimate their position, flux and incorporated them in the background fit (discussed in Section 2.1.2).

We extracted spectra from four concentric annuli, $0' - 2'$, $2' - 4'$, $4' - 6'$, and $6' - 8.6'$ for the central pointing. We extracted spectra from two partial annuli $12.4' - 29'$, $29' - 48.3'$ for the pointings in the north direction and from $8.6' - 26'$, $26' - 45'$ for the pointings in the east direction. For the north-east direction, we extracted spectra from a partial annulus of $27' - 42'$. All annuli had widths ranging from 8 kpc at the central region to 223 kpc at the outermost bin. We generated redistribution matrix files (RMF) for all regions and detectors using *FTOOL xisrmfgen* and instrumental background files (NXB) using *FTOOL xisnxbgen*. The ancillary response files (ARF) were generated using *xissimarfgen* by providing an appropriate β -image derived from the *Chandra* surface brightness profile of MKW4 at the central region. Another ARF was produced to model the X-ray background by considering uniform sky emission in a circular region of $20'$ radius. An exposure corrected and NXB subtracted mosaic image of MKW4 in the 0.5-2 keV energy band is shown in Figure 1. We obtained *Suzaku* surface brightness profiles of MKW4 in three different directions, as shown in Figure 2. We fitted the profiles with a single β -model (Arnaud 2009):

$$S(r) = S_0 \left[1 + \left(\frac{r}{r_c} \right)^2 \right]^{-3\beta+1/2}, \quad (2)$$

which yielded the best-fit $(\beta, r_c) = (0.515 \pm 0.001, 30 \pm 2.5$ kpc).

[‡] <http://ned.ipac.caltech.edu>

[§] <https://heasarc.gsfc.nasa.gov/docs/suzaku/analysis/abc/>

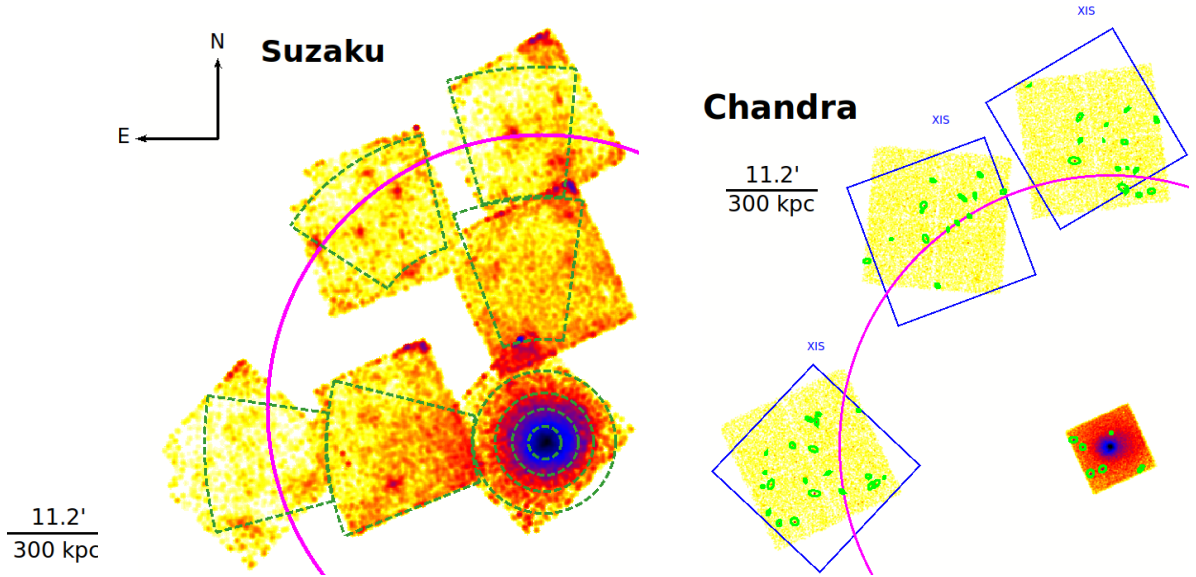


Figure 1. Left: *Suzaku* mosaic image of MKW4 in the 0.5-2 keV energy band with NXB subtracted and exposure corrected. Green annuli represent the regions used for spectra extraction. Magenta circle indicates $R_{200} = 33.2'$ (884 kpc). Right: *Chandra* mosaic image of MKW4 center (ACIS-S3) and three outer regions (ACIS-I) in the 0.5-2.0 keV energy band. The image of MKW4 is smoothed with a Gaussian kernel and a number of radii of 30. Blue boxes represent the *Suzaku* FOV. Green elliptical regions are the resolved point sources. Magenta circle indicates R_{200} .

Table 1. Observational log

Name	Obs Id	Instrument	Obs Date	Exposure time (ks)	RA ($^{\circ}$)	DEC ($^{\circ}$)	P.I.
<i>Suzaku</i> central	808066010	XIS0, XIS1, XIS3	2013 Dec 30	34.6	181.1346	1.9097	F. Gastaldello
<i>Suzaku</i> Offset 1	805081010	XIS0, XIS1, XIS3	2010 Nov 30	77.23	181.1270	2.2181	F. Gastaldello
<i>Suzaku</i> N2	808067010	XIS0, XIS1, XIS3	2010 Nov 30	97	181.1504	2.5206	Y. Su
<i>Suzaku</i> Offset 2	805082010	XIS0, XIS1, XIS3	2010 Nov 30	80	181.4270	1.8972	Y. Su
<i>Suzaku</i> E1	808065010	XIS0, XIS1, XIS3	2013 Dec 29	100	181.7142	1.8506	F. Gastaldello
<i>Suzaku</i> NE	809062010	XIS0, XIS1, XIS3	2013 Dec 29	87.5	181.4583	2.3361	Y. Su
<i>Chandra</i> central	3234	ACIS-S	2002 Nov 24	30	181.1283	1.9286	Y. Fukazawa
<i>Chandra</i> N	20593	ACIS-I	2019 Feb 25	14	181.1369	2.5209	Y. Su
<i>Chandra</i> E	20592	ACIS-I	2018 Nov 17	15	181.7146	1.8715	Y. Su
<i>Chandra</i> NE	20591	ACIS-I	2019 Mar 08	14	181.4548	2.3585	Y. Su

2.1.2 Spectral analysis

Spectral analysis was performed using XSPEC-12.10.1 and C-statistics. Each spectrum was rebinned to guarantee 20 photons per bin to aid the convergence and the computational speed. Spectra extracted from the XIS0, XIS1, and XIS3 were simultaneously fitted. The spectral fitting was restricted to the 0.4 - 7.0 keV energy band for XIS1, and to the 0.6 - 7.0 keV energy band for XIS0 and XIS3 (e.g., Mitsuda et al. 2007). We fitted each spectrum with an ICM emission model plus a multi-component X-ray background model. The ICM emission model contains a thermal *apec* component associated with a photoelectric absorption (*phabs*) component - $\text{phabs} \times \text{apec}$, as shown in Figure 3. The temperature, abundance, and normalization of the *apec* component were allowed to vary independently for regions at the group center and at the intermediate radii. For those three regions at R_{200} , we find it necessary to fix their abundances at $0.2 Z_{\odot}$. Similar metallicity was observed at R_{200} for the RX J1159+5531 group (Su et al. 2015). We discuss the systematic uncertainties caused by this choice of abundance in Section 4.

To model the X-ray background, we adopted

$\text{phabs} \times (\text{pow}_{\text{resolved CXB}} + \text{pow}_{\text{unresolved CXB}} + \text{apec}_{\text{MW}}) + \text{apec}_{\text{LHB}}$, where $\text{pow}_{\text{resolved CXB}}$ and $\text{pow}_{\text{unresolved CXB}}$ are the power-law components to model the resolved CXB and unresolved CXB, respectively. The thermal *apec*_{MW} and *apec*_{LHB} represent two foreground components to account for emissions from the Milky Way (MW) and Local Hot Bubble (LHB), respectively. We made use of the *Chandra* observations that cover the *Suzaku* pointings of the outskirts of MKW4 to mitigate much of the CXB contribution. We detected a total of 78 point sources with *Chandra* (see Figure 1). Point sources that fall onto the ACIS-S1, S2, and S4 chips are not included in our analysis. The faintest point source was detected at a flux of $8.1 \times 10^{-15} \text{ erg cm}^{-2} \text{ s}^{-1}$. We converted the count rates of resolved point sources to the fluxes assuming a power-law model with a photon index of 1.41 (De Luca & Molendi 2004). We produced mock *Suzaku* observations for the resolved point sources using *xissim*, based on their positions and fluxes determined with *Chandra*. An exposure time of 100 ks was set to ensure good photon statistics. We extracted spectra from the mock *Suzaku* observations using the same extraction regions used for the actual *Suzaku* observations. Figure 4 (left) compares the surface brightnesses of the actual point sources resolved by *Chandra* and

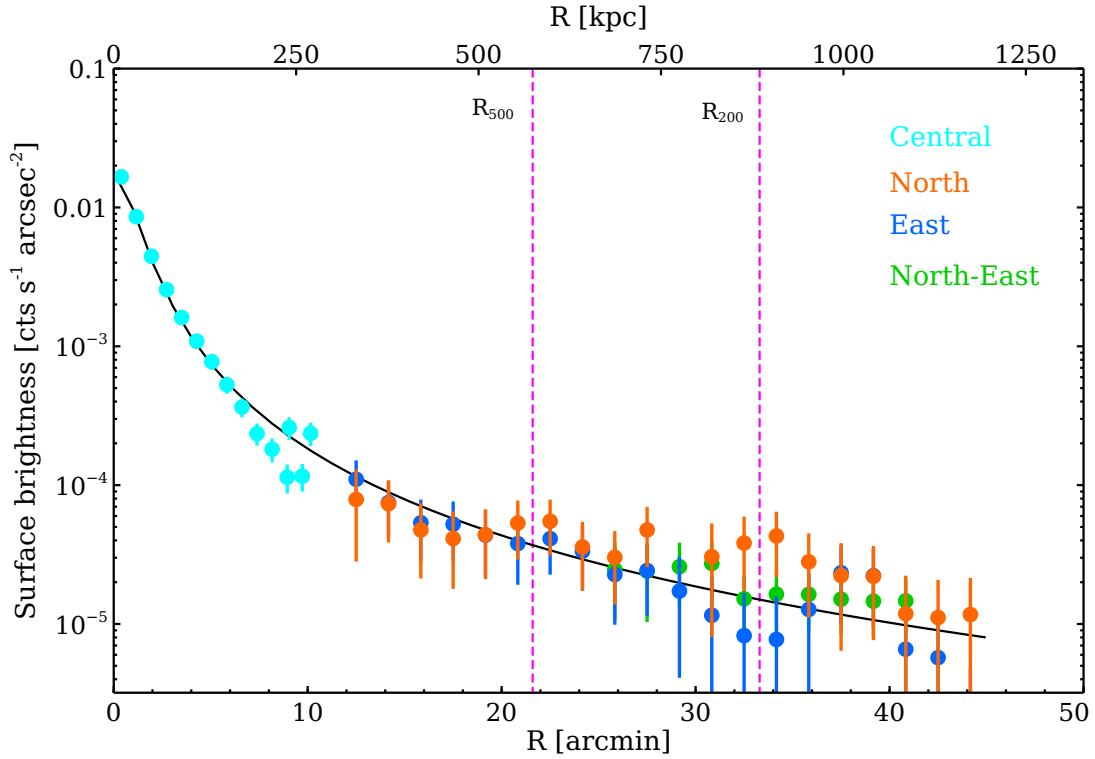


Figure 2. Surface brightness profiles of MKW4 derived from the *Suzaku* XIS image in the 0.5 - 2.0 keV energy band in three different directions. The profiles have been corrected for exposure, instrumental background (NXB), and the point sources detected with *Chandra*. Black solid line is the best-fit β -profile.

that of the simulated *Suzaku* observations, which are in good agreement with each other. We fitted the mock spectra with an absorbed power-law model (`phabs × pow`) with a photon index of 1.41. The resulting best-fit normalizations were used as the normalizations of the resolved component (`powresolved CXB`) in the background model and kept frozen. Figure 4 (*right*) compares the spectral temperature profiles (discussed in Section 3) obtained with *Suzaku* observations alone and with joint *Suzaku* and *Chandra* observations of MKW4 in the north-east direction. The significant improvement of uncertainties demonstrates that the addition of *Chandra* observations can help to constrain the CXB and increase the accuracy of the measurement of ICM properties at the outskirts (e.g., Miller et al. 2012). For the regions with no *Chandra* coverages (two regions of intermediate radii in north and east directions), we let the normalizations of `powresolved CXB` component to vary independently.

The normalizations of `powunresolved CXB` component were allowed to vary collectively for different regions, assuming little fluctuations in the surface brightness of the remaining unresolved point sources. We obtained a best-fit normalization of $4.2 \times 10^{-12} \text{ erg cm}^{-2} \text{ s}^{-1} \text{ deg}^{-2}$ for the unresolved point sources in the 2.0 - 10.0 keV energy band, as shown in Figure 4. The normalization of unresolved CXB can be estimated as (Moretti et al. 2009) -

$$F_{\text{CXB}} = 2.18 \pm 0.13 \times 10^{-11} - \int_{S_{\min}}^{S_{\max}} \left(\frac{dN}{dS} \right) \times S dS, \quad (3)$$

in units of $\text{erg cm}^{-2} \text{ s}^{-1} \text{ deg}^{-2}$, assuming a total CXB surface brightness of $2.18 \pm 0.13 \times 10^{-11} \text{ erg cm}^{-2} \text{ s}^{-1} \text{ deg}^{-2}$ in the 2.0 - 10.0 keV energy band. We adopted an analytical form of the integral source

flux distribution from Moretti et al. (2003) -

$$N(> S) = N_{\text{S(H)}} \left[\frac{(2 \times 10^{-15})^{\alpha_{1,\text{S(H)}}}}{S^{\alpha_{1,\text{S(H)}}} + S_{0,\text{H}}^{\alpha_{1,\text{S(H)}} - \alpha_{2,\text{S(H)}}} S^{\alpha_{2,\text{S(H)}}}} \right], \quad (4)$$

where $\alpha_{1,\text{S(H)}} = 1.57^{+0.10}_{-0.08}$, $\alpha_{2,\text{S(H)}} = 0.44^{+0.12}_{-0.13}$, $S_{0,\text{H}} = 4.5^{+3.7}_{1.7} \times 10^{-15} \text{ erg cm}^{-2} \text{ s}^{-1}$, and $N_{\text{S(H)}} = 5300^{+2850}_{-1400}$ are the best-fit parameters with a 68% confidence level. We estimated the flux limit for unresolved point sources to be $6.61 \pm 3.68 \times 10^{-12} \text{ erg cm}^{-2} \text{ s}^{-1} \text{ deg}^{-2}$. This flux is consistent with the flux obtained from spectral fitting.

To constrain the temperature and surface brightness of Local Hot Bubble (`apexLHB`) and Milky Way (`apexMW`) foregrounds, we used the ROSAT All-Sky Survey (RASS) data in an annulus region of 0.9° - 1.2° from the group center where no group emission was expected. We extracted spectra using the HEASARC X-ray background tool[‡]. The RASS spectrum was fitted simultaneously with the *Suzaku* data. The background fitting results are shown in Figure 3 and listed in Table 2.

2.2 Chandra

MKW4 was observed using *Chandra* with one ACIS-S pointing at the group center and three ACIS-I pointings overlapping with the

[‡] <http://heasarc.gsfc.nasa.gov/cgi-bin/Tools/xraybg/xraybg.pl>

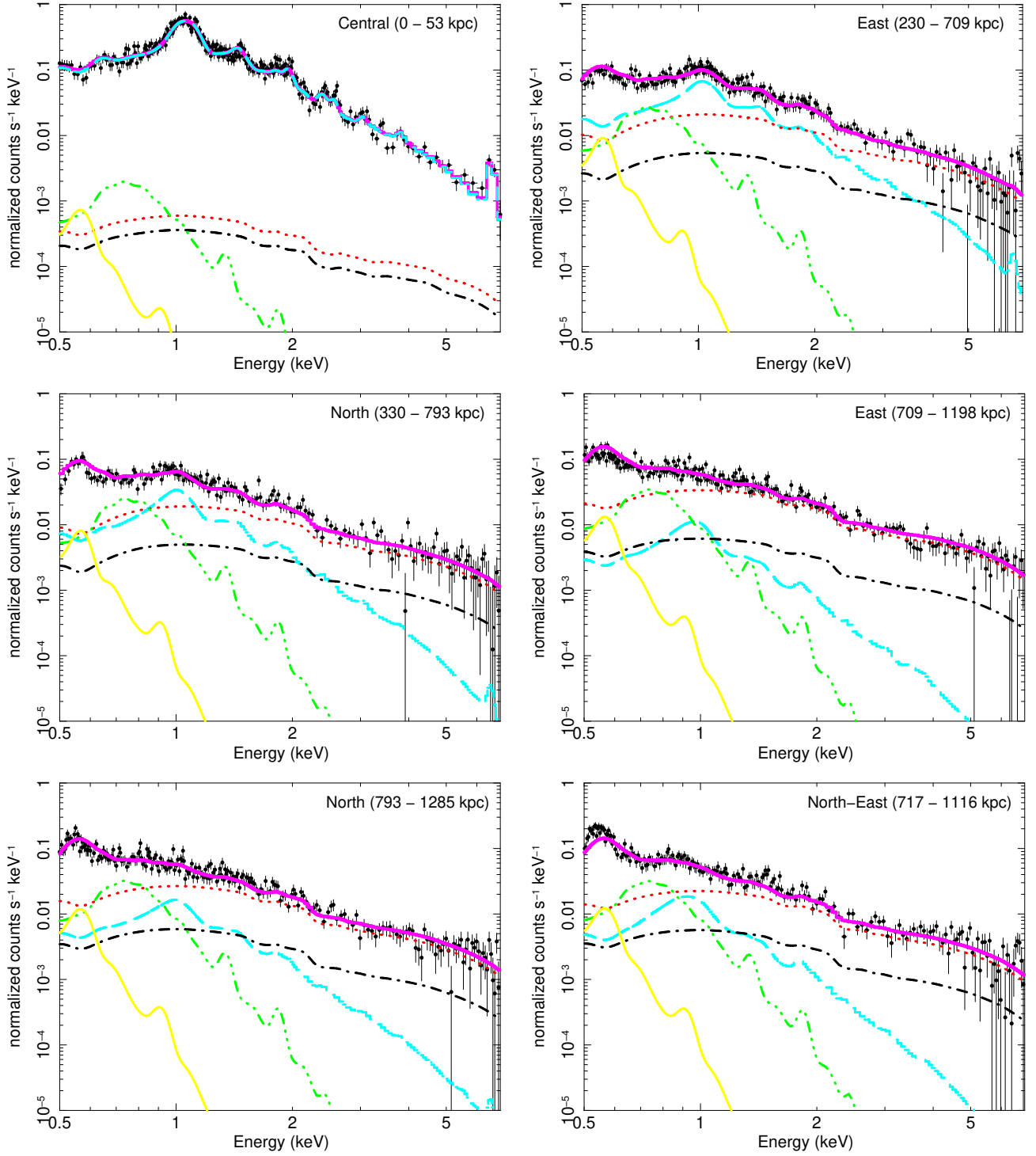


Figure 3. *Suzaku* XIS 1 spectra of MKW4 for representative regions of central and two outer bins in north and east directions. Black dots are the data points. Cyan, red, black, green, and yellow lines are the best-fit ICM emission, resolved CXB, unresolved CXB, MW, and LHB components, respectively. Magenta line is the model of the best-fit ICM emission and X-ray background components together.

outer regions observed with *Suzaku*. The observation logs are listed in Table 1.

2.2.1 Data reduction

The *Chandra* data reduction was performed using HEASoft 6.25, CIAO-4.11, and a *Chandra* calibration database (CALDB 4.8.3). We

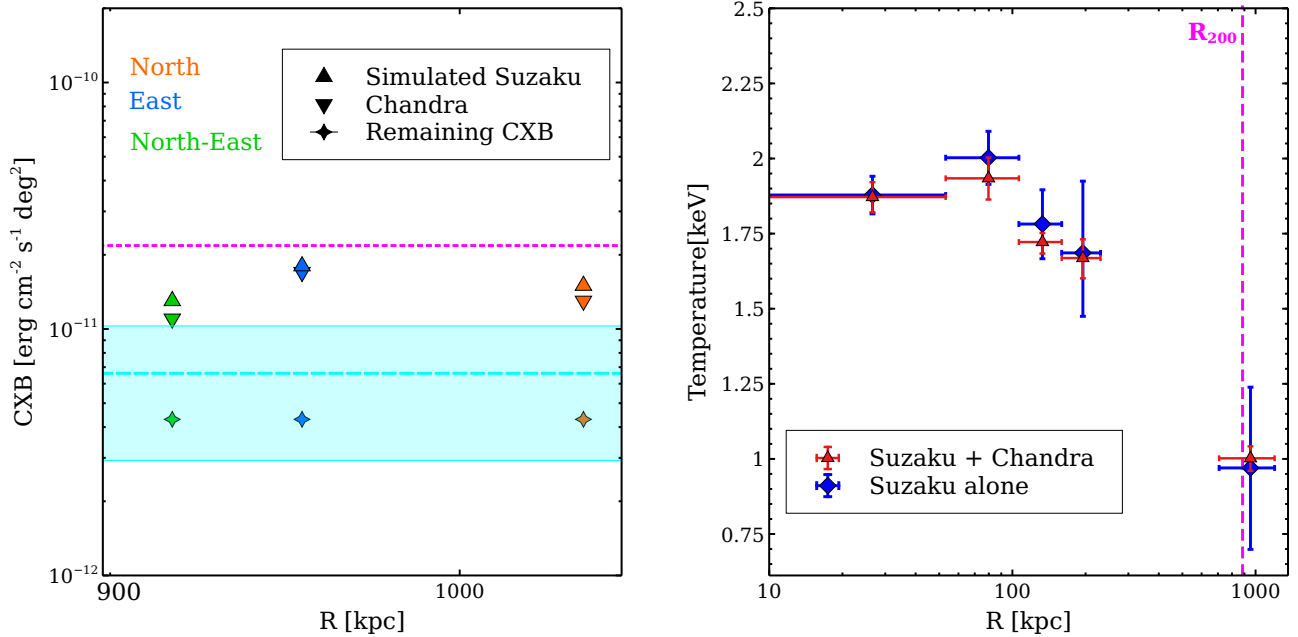


Figure 4. *Left:* Triangle down: surface brightness of point sources resolved by *Chandra*. Triangle up: surface brightness of point sources obtained from mock *Suzaku* sky. Magenta dotted: total surface brightness limit of resolved+unresolved point sources taken from [Moretti et al. \(2009\)](#). Cyan dashed: expected surface brightness limit of unresolved point sources with 1σ error (shaded) calculated using Equations 3 and 4. Star: estimated surface brightness of unresolved point sources from *Suzaku* fitting. *Right:* Blue: spectroscopic temperature profile of MKW4 in the north-east direction obtained from spectral fitting of the *Suzaku* data only. Red: same profile obtained from the joint fitting of *Suzaku* and *Chandra* data. Magenta dashed line indicates R_{200} of MKW4.

Table 2. X-ray background components of outer regions^a

Name	CXB ^b	LHB ^c	MW ^d
<i>Suzaku</i> East	$11.25^{+0.12}_{-0.13}$	$13.9^{+1.1}_{-1.3}$	$6.21^{+0.32}_{-0.35}$
<i>Suzaku</i> North	$9.51^{+0.12}_{-0.12}$	–	–
<i>Suzaku</i> North-East	$8.63^{+0.12}_{-0.12}$	–	–

^a Results for the normalizations of various components (non-instrumental) of X-ray background for a circular region with $20'$ radii. The LHB and MW components for *Suzaku* North and *Suzaku* North-East directions are linked to the *Suzaku* East.

^b Normalization of power-law component ($\Gamma=1.41$) for resolved + unresolved cosmic X-ray background in the units of 10^{-4} photons s^{-1} cm^{-2} keV^{-1} at 1 keV.

^c Normalization of the unabsorbed *apec* thermal component ($kT = 0.08$ keV, $abun = 1Z_{\odot}$) integrated over line of sight, $1/4\pi [D_A(1+z)]^2 \int n_e n_H dV$ in the units of 10^{-18} cm^{-5} .

^d Normalization of the absorbed *apec* thermal component ($kT = 0.2$ keV, $abun = 1Z_{\odot}$) integrated over line of sight, $1/4\pi [D_A(1+z)]^2 \int n_e n_H dV$ in the units of 10^{-18} cm^{-5} .

followed a standard data reduction thread [§]. All data were reprocessed from the level 1 events using *chandra_repro*, which applied the latest gain, charge transfer inefficiency correction, and filtering from bad grades. The light curves were filtered using *1c_clean* script to remove periods affected by flares. The resulting filtered exposure times are listed in Table 1. Point sources were identified with

wavdetect using a range of wavelet radii between 1 and 16 pixels to maximize the number of detected point sources. The detection threshold was set to 10^{-6} , which guaranteed detection of $\lesssim 1$ spurious source per CCD. Detected point sources were confirmed visually. Figure 1 shows the adaptively smoothed ACIS-S3 image of MKW4 in the 0.5 - 2.0 keV energy band.

We extracted spectra from 6 adjoining, concentric annuli centered at the X-ray centroid in the *Chandra* ACIS-S3 chip. The widths of the annular regions were chosen to contain approximately the same number of background-subtracted counts of 2000 for better spectral analysis. Count-weighted spectral response matrices (ARFs and RMFs) were generated using *mkwarf* and *mkaci_srmf* tasks for each annulus. The blanksky background was produced by the *blanksky* tool for background subtraction. The blanksky background was tailored based on the count rate in the 9.5 - 12.0 keV energy band relative to the observation.

2.2.2 Spectral analysis

All spectra were fitted simultaneously to model the ICM properties of different regions. We modeled the ICM emission with a single thermal *apec* model associated with a photoelectric absorption model- *phabs* \times *apec*. Photoionization cross-sections were taken from [Balucinska-Church & McCammon \(1992\)](#). We obtained the galactic hydrogen column density, $N_H = 1.72 \times 10^{20}$ cm^{-2} at the direction of MKW4, using HEASARC N_H tool ^{††}. All ICM emission components were allowed to vary independently.

[§] <http://cxc.harvard.edu/ciao/threads/index.html>

^{††} <http://heasarc.gsfc.nasa.gov/cgi-bin/Tools/w3nh/w3nh.pl>

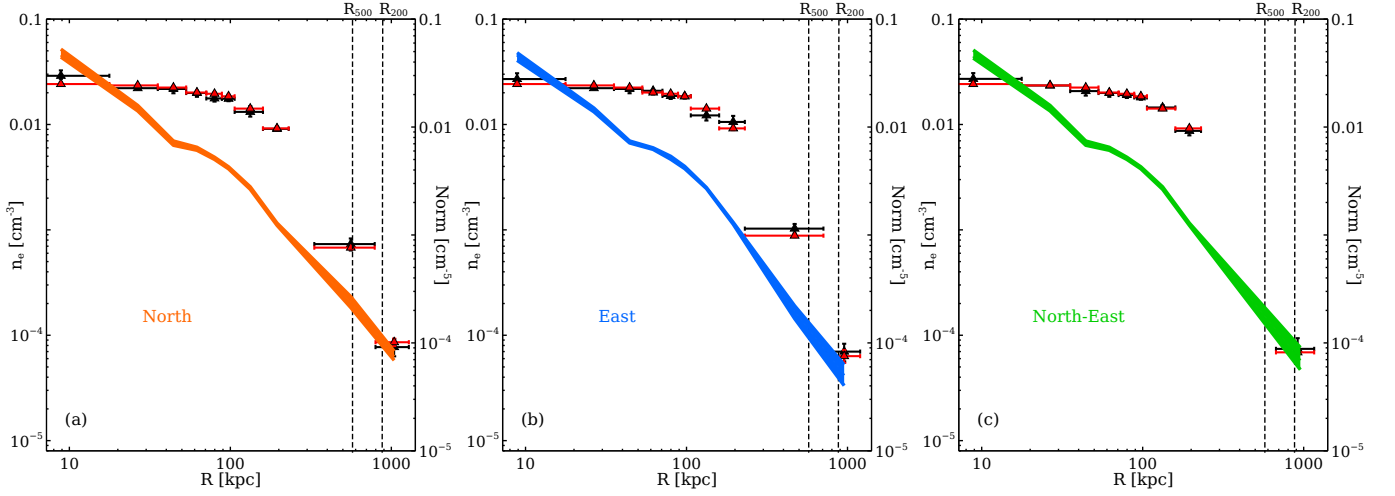


Figure 5. Deprojected density profiles of MKW4 in north (orange), east (blue), and north-east (green) directions. Shaded regions indicate 1σ uncertainties. Red triangles: the best-fit normalizations for the *apec* thermal component obtained from spectral analysis. Black triangles: the normalizations of the *apec* thermal component calculated from the resulting 3D density profile.

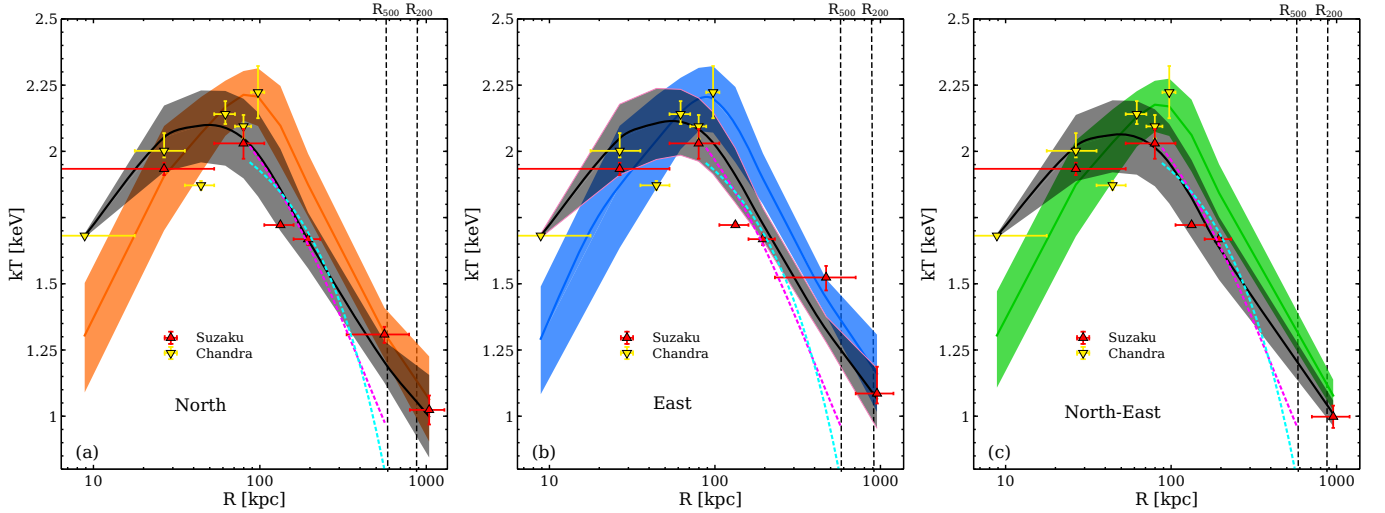


Figure 6. Deprojected temperature profiles of MKW4 in north (orange), east (blue), and north-east (green) directions. The 2D temperature profiles of MKW4, estimated using Equation 6, are indicated in black. Shaded regions indicate 1σ uncertainties. Temperatures obtained from the *apec* thermal component by fitting the spectra extracted from the *Chandra* and *Suzaku* data are shown in yellow and red respectively. Magenta and cyan dashed lines show the average temperature profiles derived for groups in Loken et al. (2002) and Sun et al. (2009) respectively.

3 RESULTS

3.1 Density and temperature profile

We derive the deprojected (3D) gas density and temperature profiles of MKW4 assuming analytical prescriptions for 3D gas density and temperature. We follow the analytical expressions described in Vikhlinin et al. (2006). The normalization of the *apec* thermal component relates to the ICM density as: $\text{norm} = \int n_e n_p dl$, where the density profile of electrons (n_e) and protons (n_p) can analytically be described as:

$$n_e n_p(r) = \frac{n_{01}^2}{\left(1 + r^2/r_{c1}^2\right)^{3\beta_1}} + \frac{n_{02}^2}{\left(1 + r^2/r_{c2}^2\right)^{3\beta_2}}. \quad (5)$$

We obtain the 3D density profile of MKW4 by projecting the 3D analytic model given in Equation 5 along the line of sight and fit it to the measured 2D normalizations of thermal *apec* component obtained from the spectral analysis, assuming $n_e = 1.2n_p$ and a fixed $\gamma = 3$. The uncertainties are calculated using Monte Carlo simulations with 1000 to 2000 realizations.

The resulting 3D density profiles are shown in Figure 5. A comparison between the normalizations obtained from spectral analysis and the normalizations obtained from the Equation 5 are also shown in Figure 5. Figure 7 compares the 3D density profiles of MKW4 in three different directions.

We derive the 3D temperature profile by fitting the spectral temperature (2D spectroscopic temperature, T_{2D}) obtained from thermal *apec* component with the following analytic function (Vikhlinin et al.

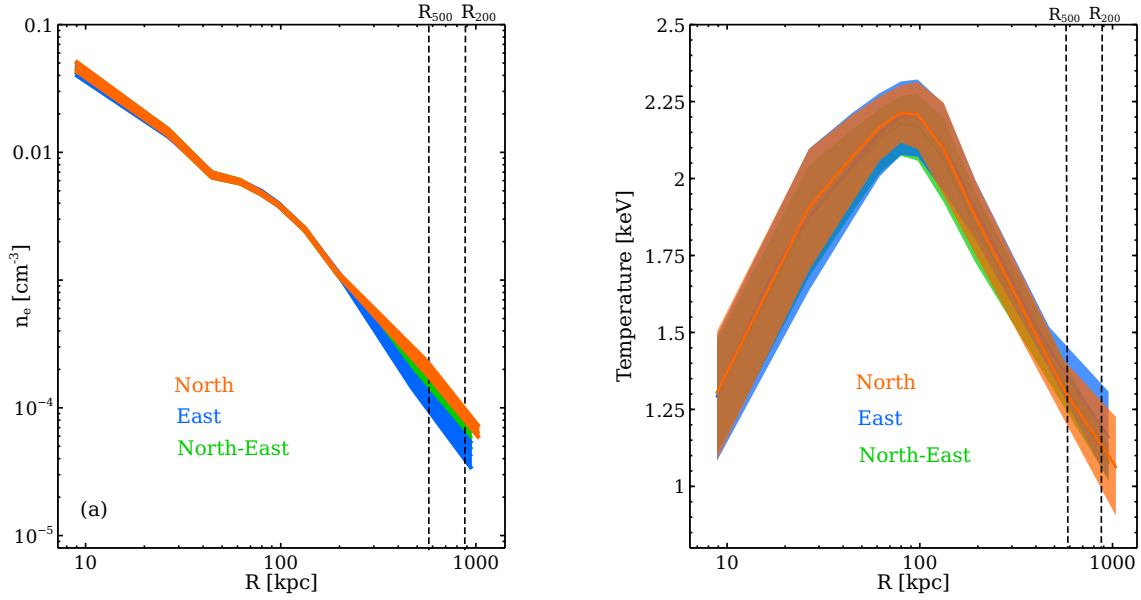


Figure 7. 3D density (left) and temperature (right) profiles of MKW4 in three different directions.

2006):

$$T_{2D} = \frac{\int n_e^2 T_{3D}^{\frac{1}{4}} dV}{\int n_e^2 T_{3D}^{-\frac{3}{4}} dV}, \quad (6)$$

where

$$T_{3D}(r) = T_0 \frac{(x + T_{\min}/T_0)}{(x + 1)} \times \frac{(r/r_t)^{-a}}{(1 + r^b/r_t^b)^{c/b}}, \quad (7)$$

and $x = \left(\frac{r}{r_{\text{cool}}}\right)^{a_{\text{cool}}}$.

Figure 6 represents the projected (T_{2D}) and deprojected (T_{3D}) temperature profiles of MKW4 from its center out to the virial radii in north, east, and north-east directions.

The uncertainties in temperatures are also calculated using Monte Carlo simulations. The deprojected temperature profiles of MKW4 decline from 2.20 keV at $0.1R_{200}$ to 1.14 keV at R_{200} . A similar temperature drop was found in other groups (e.g., [Su et al. 2015](#)). The projected temperatures measured with *Suzaku* and *Chandra* are consistent for the overlapping regions. Figure 7 compares the 3D temperature profiles of MKW4 in three different directions.

Our temperature profile agrees well with the *Chandra* temperature profiles of MKW4 out to R_{2500} , as given by [Vikhlinin et al. \(2006\)](#) (V06) and [Sun et al. \(2009\)](#) (S09) as well as the measurement obtained with *XMM-Newton* by [Gastaldello et al. \(2007\)](#) (G07) out to $\sim 0.6R_{500}$. We measure a gas temperature at R_{500} between those of V06 and S09 and consistent with the *Suzaku* measurement using the two intermediate pointings ([Sasaki et al. 2014](#)). We compare the projected temperature profiles of MKW4 to the empirical profiles derived for groups by [Sun et al. \(2009\)](#):

$$\frac{T}{T_{2500}} = (1.22 \pm 0.02) - (0.79 \pm 0.04) \frac{R}{R_{500}}, \quad (8)$$

and by [Loken et al. \(2002\)](#):

$$\frac{T}{T_{2500}} = (1.37 \pm 0.03) - \left(1 + \frac{R}{R_{500}}\right)^{-(1.34 \pm 0.21)}, \quad (9)$$

as shown in Figure 6. Both profiles show good agreement with the projected temperature profile of MKW4 out to $\sim R_{2500}$. Their values at R_{500} exceed what is measured for MKW4 by 30% and 60%, respectively. These empirical profiles are determined with a large number of galaxy groups with a sizable scatter. Many of them do not have their temperatures actually measured out to R_{500} .

3.2 Entropy and pressure profile

We derive the 3D entropy and pressure profiles of MKW4 from 3D density and temperature profiles, as shown in Figures 8 and 9.

We compare our entropy profiles with a baseline profile derived from purely gravitational structure formation ([Voit et al. 2005](#)) and assuming a hydrostatic equilibrium-

$$K_{\text{gra}}(R) = 1.32 K_{200} \left(\frac{R}{R_{200}}\right)^{1.1}, \quad (10)$$

and the normalization K_{200} is defined as-

$$K_{200} = 362 \frac{G M_{200} \mu m_p}{2R_{200}} \left(\frac{1}{\text{keV}}\right) E(z)^{-4/3} \times \left(\frac{\Omega_m}{0.3}\right)^{-4/3} \text{keV cm}^{-2}, \quad (11)$$

$$\text{where, } E(z) = \sqrt{\Omega_m (1+z)^3 + \Omega_\Lambda}. \quad (12)$$

The m_p is proton mass and $\mu \sim 0.6$ is the mean molecular weight. The 3D entropy profiles of MKW4 increase monotonically with radius in three directions, as seen in Figure 8. We observe apparent entropy excesses towards the central region (up to $\sim 0.5R_{200}$) of MKW4 relative to the baseline profile. At larger radii, the entropy profiles of MKW4 are consistent with the baseline profile, i.e., its slope attains a value of ~ 1.1 between R_{500} and R_{200} in all observed directions.

The 3D pressure profiles of MKW4 are shown in Figure 9. We

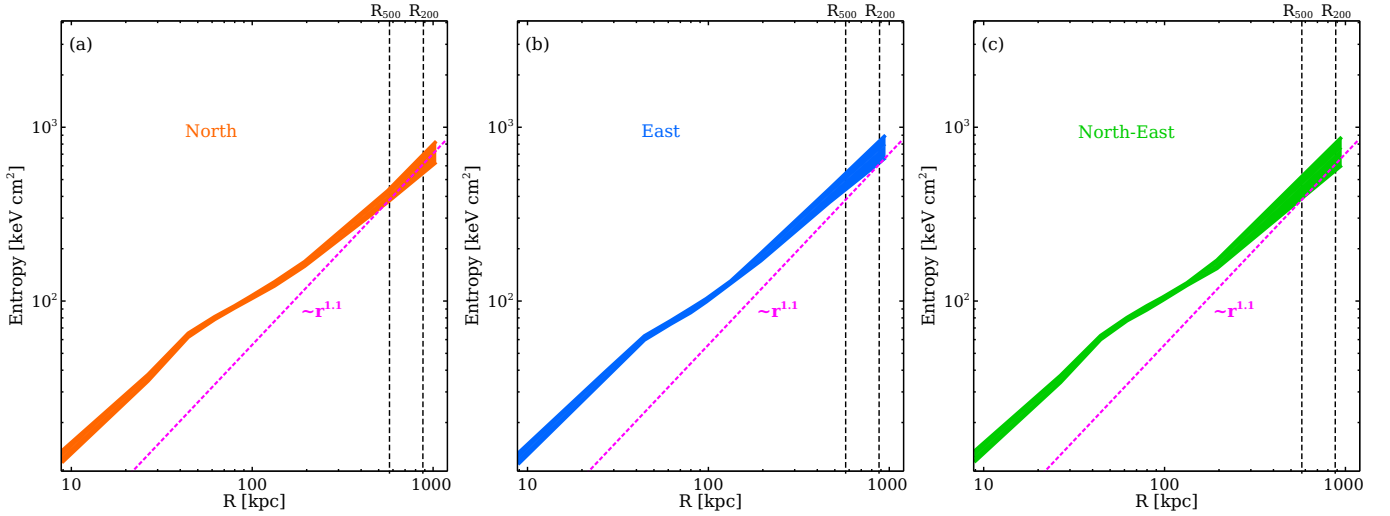


Figure 8. 3D entropy profiles of MKW4 in north (orange), east (blue), and north-east (green) directions. Shaded regions indicate 1σ uncertainties. Magenta dashed line represents the entropy profile derived from gravity only cosmological simulation (Voit et al. 2005) using Equation 10.

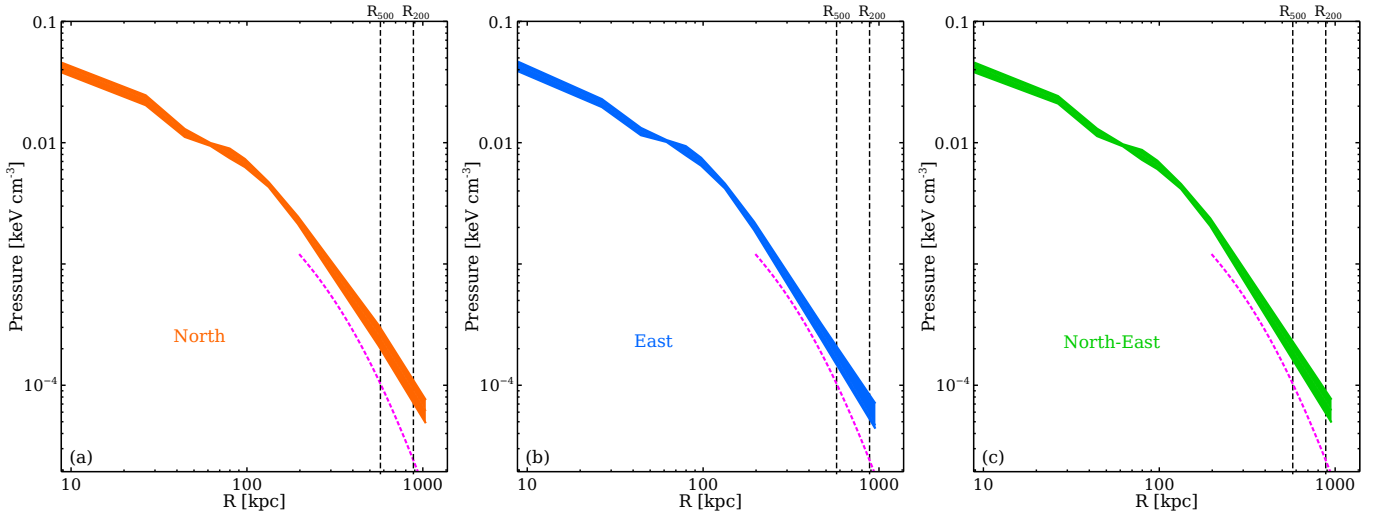


Figure 9. 3D pressure profiles of MKW4 in north (orange), east (blue), and north-east (green) directions. Shaded regions indicate 1σ uncertainties. Magenta dashed line represents the semi-analytical universal pressure profile (Arnaud et al. 2010), derived using Equation 13.

compare the measured pressure profiles to a semi-analytical universal pressure profile (Arnaud et al. 2010) defined as -

$$P(r) = P_{500} \left[\frac{M_{500}}{3 \times 10^{14} h_{70}^{-1} M_{\odot}} \right]^{\alpha_p + \alpha'_p(x)} \times \frac{P_0}{(c_{500}x)^{\gamma} [1 + (c_{500}x)^{\alpha}]^{\frac{\beta - \alpha}{\alpha}}} \quad (13)$$

where $x = \frac{R}{R_{500}}$, $\alpha'_p(x) = 0.10 - (\alpha_p + 0.10) \frac{(x/0.5)^3}{[1 + (x/0.5)^3]}$. The P_{500} is the pressure at R_{500} and M_{500} (see Table 3) is the total hydrostatic mass within R_{500} . We adopt

$$[P_0, c_{500}, \alpha, \beta, \gamma, \alpha_p] = [8.403h_{70}^{-3/2}, 1.177, 0.3081, 1.0510, 5.4905, 0.12 \pm 0.10]$$

from Arnaud et al. (2010). Sun et al. (2011) adopted similar parameters and found that the Arnaud et al. (2010) pressure profile is also representative for galaxy groups. The 3D pressure profiles of

MKW4 in all directions from $0.35R_{500}$ out to $\sim 0.65R_{500}$ show good agreement with this universal pressure profile but exceed it by more than 50% at R_{500} .

3.3 Mass and gas fraction

We derive the X-ray hydrostatic mass of MKW4 and its gas mass within a specific radius (R) from the group center, incorporating the above 3D density and temperature profiles in the following equations-

$$M_{\text{tot}}(< R) = - \frac{kT_{3D}R}{G\mu m_p} \left(\frac{d \ln \rho_{\text{gas}}}{d \ln R} + \frac{d \ln T_{3D}}{d \ln R} \right) \quad (14)$$

$$M_{\text{gas}}(< R) = 4\pi \int_0^R \rho_g(r') r'^2 dr', \quad (15)$$

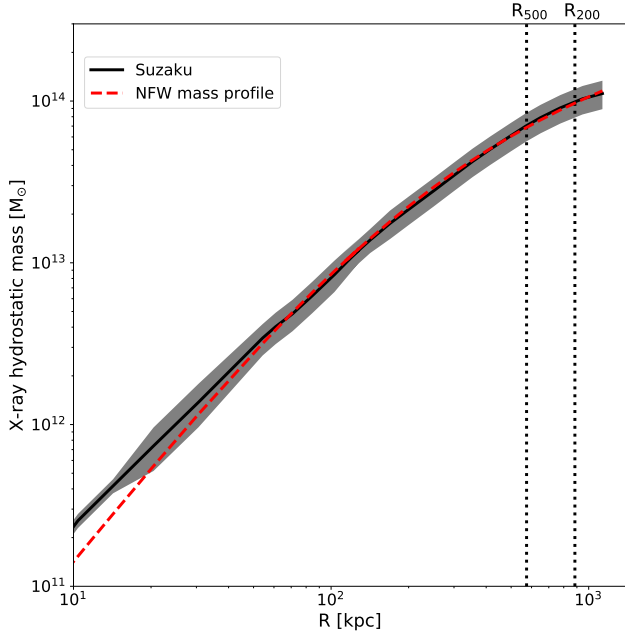


Figure 10. The X-ray hydrostatic mass profile (M_{total}) of MKW4 derived using Equation 14. Red dashed line shows best-fit NFW mass profile obtained by integrating Equation 16. Shaded region indicates 1σ error.

where $\rho_{\text{gas}} = 1.92\mu_{\text{H}}n_{\text{e}}$ is the gas density, and m_{H} is the proton mass. The resulting hydrostatic mass profile of MKW4 is shown in Figure 10. We obtain $M_{\text{tot}}(< R_{500}) \approx 6.5 \pm 1.0 \times 10^{13} M_{\odot}$ and $M_{\text{tot}}(< R_{200}) \approx 9.7 \pm 1.5 \times 10^{13} M_{\odot}$. Our measured hydrostatic mass within R_{500} is between that given by Vikhlinin et al. (2006) ($7.7 \pm 1.0 \times 10^{13} M_{\odot}$) and those of Gastaldello et al. (2007) ($4.3 \pm 0.2 \times 10^{13} M_{\odot}$) and Sun et al. (2009) ($4.8 \pm 0.7 \times 10^{13} M_{\odot}$).

We fit our hydrostatic mass profile to the NFW mass density profile (Navarro et al. 1997):

$$\rho(r) = \frac{\rho_s}{(r/r_s)(1+r/r_s)^2}, \quad (16)$$

as shown in Figure 10. We obtain a best-fit r_s of 186 ± 23 kpc, which gives the central mass concentrations of $c_{500} = 3.09^{+0.52}_{-0.39}$ at R_{500} and $c_{200} = 4.75^{+0.80}_{-0.60}$ at R_{200} . We also obtain the sparsity, the ratio of masses at two overdensities (Corasaniti et al. 2018), $S_{200,500} = 1.49 \pm 0.31$. Our measurement of $S_{200,500}$ for MKW4 is closely align with the typical $S_{200,500}$ of 1.5 found for galaxy clusters in N-body simulation (Corasaniti et al. 2018).

We obtain its enclosed gas mass and estimate the gas mass fraction $f_{\text{gas}} = \frac{M_{\text{gas}}}{M_{\text{tot}}}$ for each direction, as shown in Figure 11. At $\sim R_{500}$, the measured gas mass fraction of MKW4 is below 10% in all directions, similar to the other galaxy groups (e.g., Vikhlinin et al. 2006; Sun et al. 2009; Humphrey et al. 2012; Thölken et al. 2016). At a radii larger than R_{500} , f_{gas} grows slowly and attains a value of 0.092 ± 0.009 in the north, 0.087 ± 0.012 in the east, and 0.090 ± 0.011 in the north-east at R_{200} . These gas mass fractions are surprisingly low compared to the cosmic baryon fraction of 0.15 (Planck Collaboration et al. 2014) and 0.17 (Komatsu et al. 2011). A brief comparison of

the mass and f_{gas} of MKW4 between our work and previous studies is listed in Table 4.

4 SYSTEMATIC UNCERTAINTIES

We investigate changes of the best-fit gas density, temperature, entropy, pressure, and enclosed gas mass fraction at R_{200} introduced by a variety of systematic effects. Below we focus on the systematic uncertainties related to the entropy. All other gas properties are listed in Table 5.

We consider two different sources of systematic uncertainties associated with the CXB. First, we allow the best fit normalization of the CXB component in the background model to vary by 20% with a fixed power-law slope of $\Gamma = 1.41$ (De Luca & Molendi 2004), which leads to a maximum change in gas entropy by $\sim 18\%$ at R_{200} for the north, east, and north-east directions (see ΔCXB in Table 5). Second, we fix the CXB power-law slope to $\Gamma = 1.3$ and 1.5, respectively. Adopting $\Gamma = 1.3$ has little effect on our results for the north direction, while the gas entropy varies by $\sim 30\%$ for the other two directions. Adopting $\Gamma = 1.5$, the gas entropy is increased by $\sim 14\%$ for the north and east directions, while no significant changes are observed for the north-east direction.

We examine the impacts on gas properties due to variations in the MW and LHB foreground components by varying the normalization of each component by 10% (see ΔMW and ΔLHB in Table 5). We find that the variation in the MW component changes the gas entropy by 22% in the east and 27% in the north-east. The 10% variation in the LHB component changes the entropy by 20% in the north and 27% in the north-east.

We adopt the solar abundance table of Asplund et al. (2006) for the spectral analysis, as shown in Figure 3. Here, we experiment with two different solar abundance tables of Anders & Grevesse (1989) and Lodders (2003) to find their impacts on the measurement of gas properties. Results are listed in Table 5 under Δsolar . Using the Anders & Grevesse (1989) solar abundance table, the gas entropy increases by 20% in the north, 13% in the east, and 32% in the north-east directions. In contrast, using the Lodders (2003) abundance table, the entropy does not change significantly in the north and north-east directions but decreases by 20% in the east.

In the spectral analysis, we find it necessary to fix the ICM metallicity at $0.2 Z_{\odot}$ for regions at R_{200} . Here, we estimate the uncertainties in the measurements of gas properties associated with the possible variation of the ICM metallicity. We repeat the spectral analysis by fixing the metallicity at $0.1 Z_{\odot}$ and $0.3 Z_{\odot}$ (see Δabun in Table 5). Fixing the metal abundance at $0.1 Z_{\odot}$ has little impact on gas properties at the outskirts of MKW4, while adopting a metallicity of $0.3 Z_{\odot}$ increases the gas entropy by $\sim 20\%$ in the north, 15% in the east, and 25% in the north-east directions.

5 DISCUSSION

Combining the deep *Suzaku* observations with the *Chandra* ACIS-S and ACIS-I observations of MKW4, we measured its gas properties from the group center out to the virial radii in three directions. Its

Table 3. Properties of MKW4

T_{2500}^a (keV)	T_{500} (keV)	T_{200} (keV)	R_{2500} (kpc)	R_{500} (kpc)	R_{200} (kpc)	M_{500}^b ($10^{13} M_{\odot}$)	M_{200} ($10^{13} M_{\odot}$)	$f_{\text{gas}, 2500}^c$	$f_{\text{gas}, 500}$	$f_{\text{gas}, 200}$	c_{500}	c_{200}
$1.71^{+0.09}_{-0.08}$	1.36 ± 0.09	$1.14^{+0.16}_{-0.13}$	274 ± 10	574 ± 20	884 ± 17	6.5 ± 1.0	9.7 ± 1.5	0.05 ± 0.01	0.07 ± 0.01	0.090 ± 0.011	$3.09^{+0.52}_{-0.39}$	$4.75^{+0.80}_{-0.60}$

^a T_{Δ} = deprojected temperature at R_{Δ} .

^b M_{Δ} = total X-ray hydrostatic mass within R_{Δ} .

^c $f_{\text{gas}, \Delta}$ = enclosed gas mass fraction at R_{Δ} .

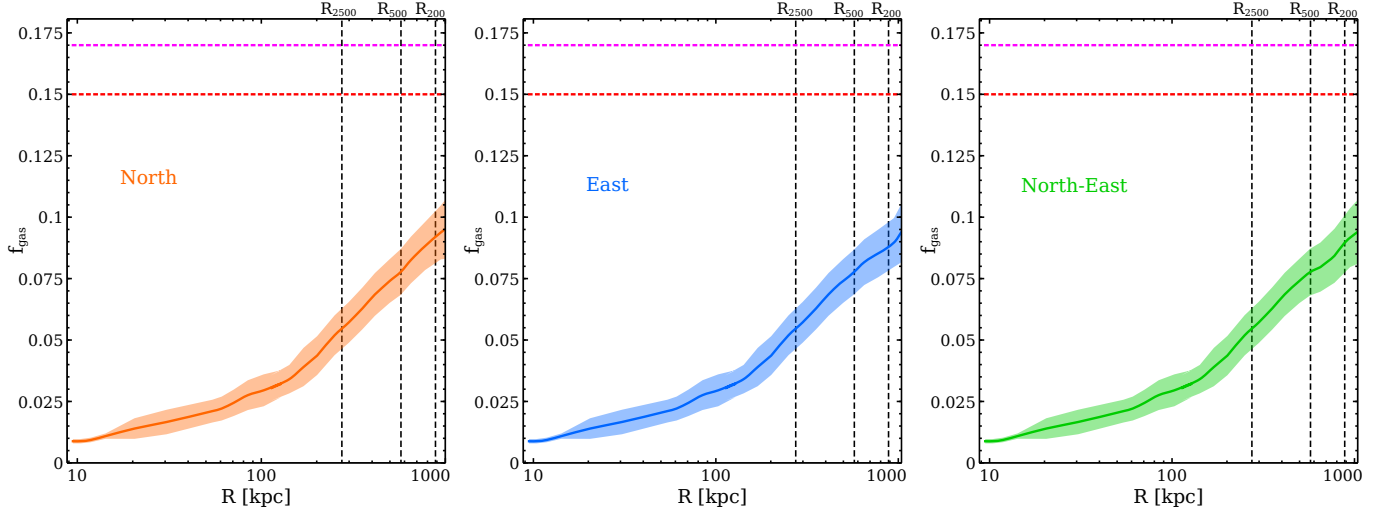


Figure 11. The gas mass fraction of MKW4 in north (orange), east (blue), and north-east (green) directions. Red dashed line: cosmic baryon fraction estimated by *Planck* (Planck Collaboration et al. 2014). Magenta dashed line: cosmic baryon fraction estimated by *WMAP* (Komatsu et al. 2011).

Table 4. Comparison of our results with other works

Name	R_{500} (kpc)	M_{500}^{\ddagger} $\times 10^{13} (M_{\odot})$	$f_{\text{gas}, 2500}^{\dagger}$	$f_{\text{gas}, 500}^{\dagger}$	c_{500}
This work	574 ± 20	6.5 ± 1.0	0.05 ± 0.01	0.07 ± 0.01	$3.09^{+0.52}_{-0.39}$
S09 [§]	538^{+24}_{-29}	$4.85^{+0.71}_{-0.68}$	$0.047^{+0.002}_{-0.003}$	0.086 ± 0.009	$3.93^{+1.16}_{-0.78}$
G07	527 ± 8	4.27 ± 0.18	–	–	6.4 ± 0.5
V06	634 ± 28	7.7 ± 1.0	0.045 ± 0.002	0.062 ± 0.006	2.54 ± 0.15

[‡] M_{Δ} = total X-ray hydrostatic mass within R_{Δ} .

[†] $f_{\text{gas}, \Delta}$ = enclosed gas mass fraction at R_{Δ} .

[§] S09, G07, and V06 are referred to Sun et al. (2009), Gastaldello et al. (2007), and Vikhlinin et al. (2006) respectively.

entropy profiles at larger radii are consistent with the self-similar value predicted by gravitational collapse alone (Voit et al. 2005). We estimated the enclosed gas mass fraction of MKW4 as a function of radial distance from the group center and obtained a surprisingly low value within R_{200} compared to clusters. Below we discuss the implications of these results in detail.

5.1 Entropy profile

The entropy profile describes the thermal history of the ICM. Previous works on massive clusters ($T_X > 3$ keV) have measured entropy profiles that flatten between R_{500} and R_{200} and even tend to fall below the self-similar value predicted by gravitational collapse alone

(e.g., Simionescu et al. 2011; Bonamente et al. 2013; Walker et al. 2012a). The explanations proposed for the unexpected entropy profiles include clumpy ICM and electron-ion non-equilibrium, either of which can be induced as galaxy clusters accrete cold gas from cosmic filaments. Using numerical simulations, Nagai & Lau (2011) predict that massive clusters with $M_{200} > 10^{14} M_{\odot} h^{-1}$ contain a significant fraction of clumpy gas at larger radii due to frequent merging events, which biases low the entropy by overestimating the gas density. We do not observe any flattening in the entropy profiles of MKW4 between R_{500} and R_{200} . Our results suggest that the merger rate is comparably lower for MKW4 because of the shallow gravitational potential well, which makes the ICM less clumpy at its outskirts. This also supports the fact that clumping factors are smaller in the low mass clusters ($M_{200} < 10^{14} M_{\odot} h^{-1}$) and groups, as suggested by Su et al. (2015), Thölken et al. (2016), and Bulbul et al. (2016). The entropy profiles of MKW4 instead follow the baseline profile (Voit et al. 2005), indicating its gas dynamics at the outskirts may be mainly regulated by gravity.

Another explanation for entropy flattening is electron-ion thermal non-equilibrium. A shock wave resulting from any recent merger and accretion event at the outskirts tends to heat the heavy-ions faster than electrons, causing the ion temperature to exceed the electron temperature. This thermal non-equilibrium could bias low the gas entropy. Numerical simulations show that the discrepancy between electron and ion temperature is more severe in more massive and rapidly growing clusters (e.g., Avestruz et al. 2015; Walker et al. 2019). The well behaved entropy profiles of MKW4 suggest that it is a relatively undisturbed system and has experienced few recent mergers.

Table 5. Systematic error of gas properties at R_{200}

	Test	Temperature keV	Density 10^{-5} cm^{-3}	Entropy keV cm^2	Pressure $10^{-5} \text{ keV cm}^{-3}$	f_{gas}
	Best fit	1.13 ± 0.14	8.85 ± 1.5	630 ± 82	9.2 ± 2.8	0.092 ± 0.009
North	ΔCXB	+0.06, -0.04	+0.08, -0.46	-4, +176	+0.17, -0.36	± 0.004
	$\Delta\text{CXB-}\Gamma$	+0.14, -0.04	-0.24, -0.13	-26, +116	-0.8, +0.003	± 0.001
	Δabun	+0.06, -0.04	+0.22, -0.46	-22, +177	+0.03, -0.36	+0.0007, -0.008
	$\Delta\text{N}_{\text{H}}$	-0.04, +0.06	-0.22, -0.15	+31, +30	-0.09, +0.4	-0.002, +0.009
	$\Delta\text{distance}$	± 0.03	± 0.2	± 66	± 0.34	± 0.008
	ΔMW	+0.084, +0.024	+0.001, -0.19	-51, +72	+0.20, +0.16	+0.001, +0.001
	ΔLHB	± 0.09	± 0.05	± 165	± 0.16	± 0.01
	Δsolar	+0.02, +0.14	-0.66, -0.23	+159, -28	± 0.78	+0.01, +0.02
	Best fit	1.17 ± 0.15	5.6 ± 1.2	712 ± 100	6.55 ± 1.3	0.087 ± 0.012
East	ΔCXB	+0.28, -0.1	+1.52, +0.84	+71, -141	+2.4, -0.03	+0.006, -0.001
	$\Delta\text{CXB-}\Gamma$	-0.2, +0.28	+1.06, +1.27	-249, +107	-0.27, +2.08	-0.006, +0.005
	Δabun	+0.28, -0.10	+0.85, +1.55	-68, +143	-0.02, +2.44	+0.005, -0.001
	$\Delta\text{N}_{\text{H}}$	-0.01, +0.05	+0.12, +0.13	-63, -55	+0.13, +0.88	+0.003, +0.02
	$\Delta\text{distance}$	± 0.02	± 0.34	± 39	± 0.06	± 0.002
	ΔMW	-0.06, +0.16	+0.9, +0.43	-186, +167	+0.23, +0.49	-0.01, +0.03
	ΔLHB	± 0.01	± 0.62	± 82	± 0.17	± 0.001
	Δsolar	+0.06, -0.1	+0.16, +1.27	+111, -191	-0.11, +0.36	-0.003, +0.008
	Best fit	1.12 ± 0.07	6.7 ± 1.8	682 ± 134	7.54 ± 1.7	0.090 ± 0.011
North-East	ΔCXB	+0.09, -0.25	+1.2, -0.36	-5, +130	+1.4, -0.3	-0.01, -0.005
	$\Delta\text{CXB-}\Gamma$	+0.06, -0.25	-1.4, -1.27	+210, -44	-1.7, -2.8	+0.003, -0.004
	Δabun	-0.15, -0.07	-0.74, -1.8	-39, +213	-1.8, -2.6	-0.003, -0.004
	$\Delta\text{N}_{\text{H}}$	-0.05, +0.06	-0.14, -0.13	-34, +40	-0.80, -0.70	-0.004, 0.007
	$\Delta\text{distance}$	± 0.05	± 1.4	± 152	± 2.1	± 0.003
	ΔMW	-0.15, +0.05	-0.67, -0.95	-61, +200	-0.93, -0.61	-0.004, -0.008
	ΔLHB	± 0.03	± 0.78	± 201	± 0.57	± 0.002
	Δsolar	-0.07, -0.25	-2.0, -1.2	+235, -60	-2.8, +2.7	± 0.004

ΔCXB : vary the normalization of the CXB component by 20%, while keeping the slope of the power law, $\Gamma = 1.4$.

$\Delta\text{CXB-}\Gamma$: set the slope of the power law for CXB component at $\Gamma = 1.3$ and 1.5 , respectively.

Δabun : set the metal abundance at $0.1 Z_{\odot}$ and $0.3 Z_{\odot}$, respectively for outermost bin.

$\Delta\text{N}_{\text{H}}$: vary the galactic hydrogen column density by 20%.

$\Delta\text{distance}$: vary the redshift parameter by 5%.

ΔMW : vary the normalization for apec_{MW} by 10%.

ΔLHB : vary the normalization for apec_{LHB} by 10%.

Δsolar : set the solar abundance table to [Anders & Grevesse \(1989\)](#) and [Lodders \(2003\)](#), respectively.

Despite the agreement between the entropy profiles of MKW4 and the baseline profile ([Voit et al. 2005](#)) at larger radii, we observe apparent entropy excess at the center of MKW4. [Pratt et al. \(2010\)](#) and [Le Brun et al. \(2014\)](#) advocate that the AGN feedback could elevate entropy profiles at the center of galaxy clusters by pushing a substantial fraction of baryons out of R_{200} . [Pratt et al. \(2010\)](#) also corrects the entropy profiles for the redistribution of hot gas due to AGN feedback, as follows-

$$K_{\text{corrected}} = K_{\text{measured}} \times \left(\frac{f_{\text{gas}}}{f_{\text{b}}} \right)^{2/3}. \quad (17)$$

We scale the measured entropy profile of MKW4 in north direction as Equation 17, adopting a cosmic baryon fraction of $f_{\text{b}} = 0.15$ from the [Planck Collaboration et al. \(2014\)](#), as shown in Figure 12. We find the scaled entropy profile follows closely with the baseline profile, even out to the virial radii, suggesting that the redistribution of the group gas due to the AGN feedback may have shaped its gas entropy ([Mathews & Guo 2011](#)).

5.2 Gas mass fraction

The enclosed gas mass fraction (f_{gas}) of MKW4 slowly rises from the group center and reaches $\sim 7\%$ within R_{500} , consistent with the

previous *Chandra* studies of MKW4 ([Vikhlinin et al. 2006](#)) and the f_{gas} of other groups (e.g., [Humphrey et al. 2012](#); [Su et al. 2013](#); [Lovisari et al. 2015](#); [Su et al. 2015](#); [Thölken et al. 2016](#)). We obtain a f_{gas} of $\sim 9\%$ within R_{200} for MKW4, which is remarkably small compared to the cosmic baryon fraction (f_{b}) of 15%. We estimate the stellar mass of MKW4 using Two Micron All-Sky Survey (2MASS[§]) data in K_{s} band, assuming a stellar mass-to-light ratio of ~ 1 ([Bell et al. 2003](#)). We find that the stellar mass contributes nearly 2% to the total hydrostatic mass, which leads to an enclosed baryon fraction (f_{b}) of $\sim 11\%$ within R_{200} of MKW4, still significantly lower than the cosmic f_{b} .

Similar discrepancies have been found in galaxies (e.g., [Fukugita et al. 1998](#); [Hoekstra et al. 2005](#); [Dai et al. 2010](#)), the so called ‘‘missing baryon problem’’, which remains a grand challenge problem in understanding the galaxy evolution (e.g., [Fukugita et al. 1998](#); [Dai et al. 2010](#)). In the case of MKW4, internal heating caused by AGN feedback may have pushed the hot gas towards larger radii or even expelled it from the system (e.g., [Metzler & Evrard 1994](#); [Bower et al. 2008](#)), which reduces the amount of hot gas, hence the baryon fraction. Alternatively, a significant amount of hot gas associated

[§] <https://irsa.ipac.caltech.edu/applications/2MASS/IM/interactive.html>

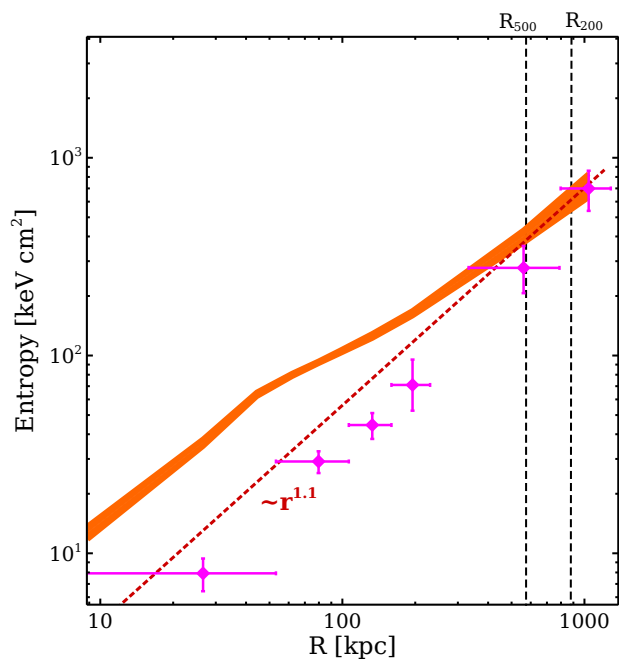


Figure 12. Orange: The entropy profile of MKW4 in north direction with 1σ error. Red: The baseline entropy profile estimated using Equation 10. Magenta: The entropy profile scaled with f_{gas} as shown in Equation 17.

with the individual galaxies may have condensed and cooled out of the X-ray emitting ICM and reside in the Circumgalactic Medium (CGM) in the form of cold gas (e.g., Fielding et al. 2017) that is undetectable in X-ray and near-infrared (K_s band). Massive systems such as clusters of galaxies typically have a f_b consistent with the cosmic f_b at the virial radii (e.g., Walker et al. 2012a; Bonamente et al. 2013), while the f_b of galaxies is approximately 7% (Hoekstra et al. 2005) at their virial radii.

We note that MKW4, as a galaxy group, has a f_b within R_{200} between those of galaxies and clusters. We compare our estimated f_{gas} at R_{200} ($f_{\text{gas},200}$) with those of other clusters and groups as a function of cluster temperature at R_{200} , as shown in Figure 13. The $f_{\text{gas},200}$ of lower-mass clusters tend to stay below the cosmic baryon fraction. In contrast, the intermediate and higher-mass clusters have $f_{\text{gas},200}$ consistent with the cosmic baryon fraction. Gravitational potential may have played a critical role in retaining hot baryons inside a galaxy cluster.

The measured $f_{\text{gas},200}$ of PKS 0745, Perseus, and A2319 exceed the cosmic baryon fraction. The $f_{\text{gas},200}$ of PKS 0745 and Perseus were measured with *Suzaku* alone, which may introduce positive bias in the gas mass measurement due to unresolved cool gas clumps at their outskirts. A2319 is a merging cluster, for which Ghirardini et al. (2018) report a substantial non-thermal pressure support at its outskirts, which may have biased the hydrostatic mass low. Our estimated $f_{\text{gas},200}$ in MKW4 is consistent with other groups of similar masses, as seen in Figure 13. The low $f_{\text{gas},200}$ found in MKW4 implies that its X-ray hydrostatic mass is unlikely to be underestimated at R_{200} .

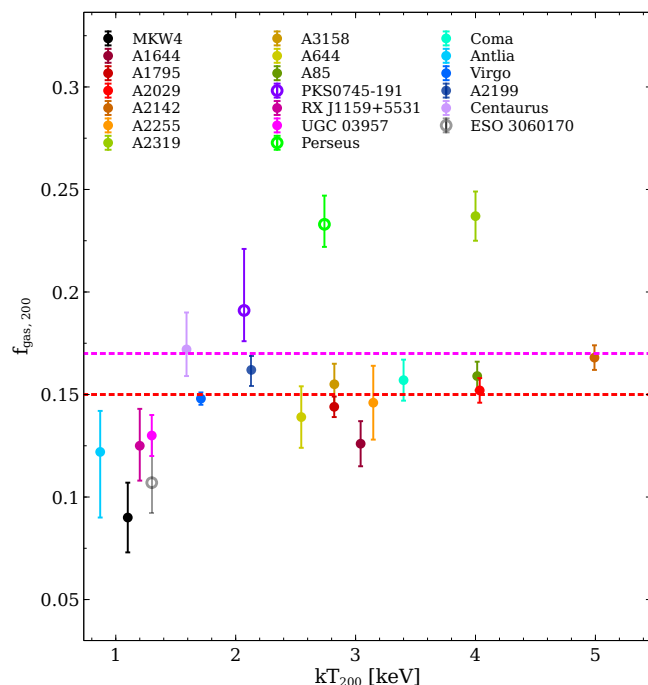


Figure 13. The f_{gas} is plotted with the cluster temperature at R_{200} . Open circles represent f_{gas} obtained using *Suzaku* only and filled circles represent f_{gas} obtained using *XMM-Newton* + *Planck* or *Suzaku* + *Chandra*. Color codes for different clusters are shown in the plot. The f_{gas} for A1644, A1795, A2029, A2142, A2255, A2319, A3158, A644, and A85 are taken from Eckert et al. (2019). We obtain f_{gas} of PKS0745-191 from Walker et al. (2012b), RX J1159+5531 from Su et al. (2015), UGC 03957 from Thölken et al. (2016), Coma from Mirakhor & Walker (2020a), Perseus from Simionescu et al. (2011), Antlia from Wong et al. (2016), Virgo from Simionescu et al. (2017), A2199 from Mirakhor & Walker (2020b), Centaurus from Walker et al. (2013), and ESO 3060170 from Su et al. (2013). Red and magenta dashed lines show cosmic baryon fraction estimated using *Planck* (Planck Collaboration et al. 2014) and *WMAP* (Komatsu et al. 2011) respectively.

5.3 Azimuthal Scatter

Azimuthal variations in the ICM properties may arise for different reasons, including unresolved substructures, mergers, and gas clumping (e.g., Miller et al. 2012; Su et al. 2015). We adopt the formula given by Vazza et al. (2011) to evaluate the azimuthal scatter of different gas properties at the outskirts of MKW4 and compare our results with the other clusters and groups-

$$S_c(r) = \sqrt{\frac{1}{N} \sum_i \frac{[y_i(r) - Y(r)]^2}{[Y(r)]^2}}, \quad (18)$$

where $y_i(r)$ is the radial profile of a quantity for the i^{th} -section, $Y(r)$ is the azimuthal average of that quantity, and N is the total number of sections. We obtain azimuthal scatters of gas properties at R_{200} of MKW4, as shown in Figure 14. We find $S_c(R_{200}) = 0.041 \pm 0.012$ in temperature, 0.191 ± 0.036 in density, 0.052 ± 0.019 in entropy, 0.149 ± 0.037 in pressure, and 0.020 ± 0.009 in the gas mass fraction.

Numerical simulations show that the azimuthal variation in gas density and temperature rises to $\sim 10\%$ at R_{200} for relaxed clusters, while it increases to $\sim 50\text{--}80\%$ for perturbed clusters (Vazza et al. 2011), as shown in Figure 14. The azimuthal scatters of the gas prop-

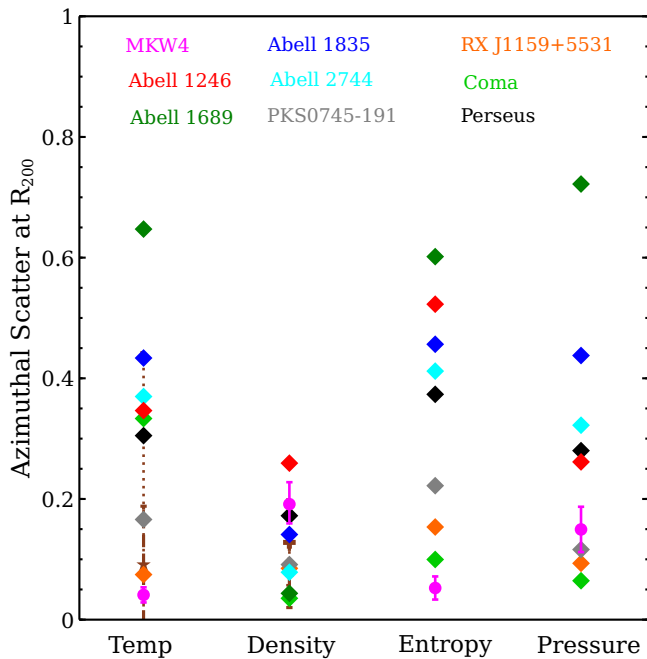


Figure 14. Azimuthal scatter of gas properties at R_{200} of MKW4. We compare our results with azimuthal variations in other clusters, e.g., A1246: Sato et al. (2014); A1689: Kawaharada et al. (2010); A1835: Ichikawa et al. (2013); A2744: Ibaraki et al. (2014); PKS0745-191: George et al. (2009); RXJ1159+5531: Su et al. (2015); Coma: Simionescu et al. (2013); Perseus: Urban et al. (2014b). Dashed brown line: the azimuthal variation in relaxed simulated clusters from Vazza et al. (2011). Dotted brown line: the azimuthal variation in perturbed simulated clusters from Vazza et al. (2011).

erties at the outskirts of MKW4 are consistent with the expectation for relaxed clusters. We also compare our results with a number of galaxy clusters observed with *Suzaku* out to R_{200} with $N = 3$ or more azimuthal coverages, as shown in Figure 14. The azimuthal variations in temperature and entropy of MKW4 are significantly smaller among those clusters. The similar ICM properties at R_{200} in the north, east, and north-east directions confirm that MKW4 is a spherically symmetric relaxed system, and the hydrostatic equilibrium is likely to be a good approximation even out to its virial radii.

6 SUMMARY

We have analysed joint *Suzaku* and *Chandra* observations of the galaxy group MKW4 and measured its ICM properties from its center out to the virial radius. We have derived the radial profiles of gas density, temperature, entropy, pressure, and gas mass fraction in three different directions. Our findings are summarized below.

- Using *Chandra* observations of MKW4, we have resolved much of the CXB at its center and three outskirt regions. We are able to model the contamination from point sources in *Suzaku* data and greatly reduce the uncertainties in the measurement of ICM properties.

- The 3D gas densities of MKW4 decline to $\sim 10^{-5} \text{ cm}^{-3}$ at its outskirts and are consistent among the three directions. The 3D

temperature profiles decline from 2.2 keV at $0.1R_{200}$ to ~ 1.14 keV at the virial radius. The temperature profiles of MKW4 in the three directions follow the universal profiles are derived by Loken et al. (2002) and Sun et al. (2009).

- The entropy profiles of MKW4 follow the baseline profile (Voit et al. 2005) beyond R_{500} in the north, east, and north-east directions, which indicates that the gas dynamics at the group outskirts is mainly regulated by the gravitational collapse. Our results also show entropy excess towards the group center compared to the baseline profile, suggesting that the central AGN of MKW4 may have redistributed the hot gas.

- We estimated the total X-ray hydrostatic mass of MKW4, $M_{\text{tot}}(< R_{500}) \approx 6.5 \pm 1.0 \times 10^{13} M_{\odot}$ and $M_{\text{tot}}(< R_{200}) \approx 9.7 \pm 1.5 \times 10^{13} M_{\odot}$. Our measurement shows that its baryon fraction is only $\sim 11\%$ at the virial radii, which is lower than the cosmic baryon fraction (Komatsu et al. 2011; Planck Collaboration et al. 2014). The lower baryon fraction implies that the central AGN feedback or galactic winds may have expelled much of its hot gas at its early epoch, or/and the hot gas associated with the individual galaxies may have condensed and cooled out of the X-ray emitting ICM and reside in the CGM in the form of cold gas.

- The azimuthal scatter in gas properties at the outskirts of MKW4 is small, suggesting that it is a remarkably relaxed system and the bulk of its ICM is likely to be in hydrostatic equilibrium.

ACKNOWLEDGEMENTS

We thank the anonymous referee for his or her helpful suggestions. A. S. and Y. S. were partially supported by the Smithsonian Astrophysical Observatory grants AR8-19020A and GO6-17125A.

DATA AVAILABILITY

The data underlying this article will be shared on reasonable request to the corresponding author.

REFERENCES

- Akamatsu H., Hoshino A., Ishisaki Y., Ohashi T., Sato K., Takei Y., Ota N., 2011, *Publications of the Astronomical Society of Japan*, 63, S1019
- Anders E., Grevesse N., 1989, *Geochimica et Cosmochimica Acta*, 53, 197
- Arnaud M., 2009, *A&A*, 500, 103
- Arnaud M., Pratt G. W., Piffaretti R., Böhringer H., Croston J. H., Pointecouteau E., 2010, *A&A*, 517, A92
- Asplund M., Grevesse N., Sauval J. A. J., 2006, *Nuclear Physics A*, 777, 1
- Avestruz C., Nagai D., Lau E. T., Nelson K., 2015, *ApJ*, 808, 176
- Balucinska-Church M., McCammon D., 1992, *ApJ*, 400, 699
- Bell E. F., McIntosh D. H., Katz N., Weinberg M. D., 2003, *ApJS*, 149, 289
- Bonamente M., Landry D., Maughan B., Giles P., Joy M., Nevalainen J., 2013, *MNRAS*, 428, 2812
- Borgani S., Finoguenov A., Kay S. T., Ponman T. J., Springel V., Tozzi P., Voit G. M., 2005, *Monthly Notices of the Royal Astronomical Society*, 361, 233

- Bower R. G., McCarthy I. G., Benson A. J., 2008, *MNRAS*, **390**, 1399
- Bulbul E., Markevitch M., Foster A., Miller E., Bautz M., Loewenstein M., Randall S. W., Smith R. K., 2016, *ApJ*, **831**, 55
- Corasanti P. S., Ettori S., Rasia Y., Sereno M., Amodeo S., Breton M. A., Ghirardini V., Eckert D., 2018, *ApJ*, **862**, 40
- Dai X., Bregman J. N., Kochanek C. S., Rasia E., 2010, *ApJ*, **719**, 119
- De Luca A., Molendi S., 2004, *A&A*, **419**, 837
- Eckert D., et al., 2019, *A&A*, **621**, A40
- Eke V. R., et al., 2004, *Monthly Notices of the Royal Astronomical Society*, **348**, 866
- Fielding D., Quataert E., McCourt M., Thompson T. A., 2017, *MNRAS*, **466**, 3810
- Fukugita M., Hogan C. J., Peebles P. J. E., 1998, *ApJ*, **503**, 518
- Gastaldello F., Buote D. A., Humphrey P. J., Zappacosta L., Bullock J. S., Brighenti F., Mathews W. G., 2007, *ApJ*, **669**, 158
- George M. R., Fabian A. C., Sanders J. S., Young A. J., Russell H. R., 2009, *Monthly Notices of the Royal Astronomical Society*, **395**, 657
- Ghirardini V., Ettori S., Eckert D., Molendi S., Gastaldello F., Pointecouteau E., Hurier G., Bourdin H., 2018, *A&A*, **614**, A7
- Hoekstra H., Hsieh B. C., Yee H. K. C., Lin H., Gladders M. D., 2005, *ApJ*, **635**, 73
- Hoshino A., et al., 2010, *Publications of the Astronomical Society of Japan*, **62**, 371
- Humphrey P. J., Buote D. A., Brighenti F., Flohic H. M. L. G., Gastaldello F., Mathews W. G., 2012, *ApJ*, **748**, 11
- Ibaraki Y., Ota N., Akamatsu H., Zhang Y. Y., Finoguenov A., 2014, *A&A*, **562**, A11
- Ichikawa K., et al., 2013, *The Astrophysical Journal*, **766**, 90
- Kawaharada M., et al., 2010, *The Astrophysical Journal*, **714**, 423
- Komatsu E., et al., 2011, *The Astrophysical Journal Supplement Series*, **192**, 18
- Le Brun A. M. C., McCarthy I. G., Schaye J., Ponman T. J., 2014, *MNRAS*, **441**, 1270
- Lodders K., 2003, *The Astrophysical Journal*, **591**, 1220
- Loken C., Norman M. L., Nelson E., Burns J., Bryan G. L., Motl P., 2002, *ApJ*, **579**, 571
- Lovisari L., Reiprich T. H., Schellenberger G., 2015, *A&A*, **573**, A118
- Mathews W. G., Guo F., 2011, *The Astrophysical Journal*, **738**, 155
- McCarthy I. G., et al., 2010, *MNRAS*, **406**, 822
- Metzler C. A., Evrard A. E., 1994, *ApJ*, **437**, 564
- Miller E. D., Bautz M., George J., Mushotzky R., Davis D., Henry J. P., 2012, in Petre R., Mitsuda K., Angelini L., eds, American Institute of Physics Conference Series Vol. 1427, American Institute of Physics Conference Series. pp 13–20 ([arXiv:1112.0034](https://arxiv.org/abs/1112.0034)), doi:10.1063/1.3696144
- Mirakhor M. S., Walker S. A., 2020a, *MNRAS*, **497**, 3204
- Mirakhor M. S., Walker S. A., 2020b, *MNRAS*, **497**, 3943
- Mitsuda K., et al., 2007, *Publications of the Astronomical Society of Japan*, **59**, S1
- Moretti A., Campana S., Lazzati D., Tagliaferri G., 2003, *ApJ*, **588**, 696
- Moretti A., et al., 2009, *A&A*, **493**, 501
- Nagai D., Lau E. T., 2011, *The Astrophysical Journal*, **731**, L10
- Navarro J. F., Frenk C. S., White S. D. M., 1997, *ApJ*, **490**, 493
- O’Sullivan E., Vrtilik J. M., Read A. M., David L. P., Ponman T. J., 2003, *MNRAS*, **346**, 525
- Paul S., John R. S., Gupta P., Kumar H., 2017, *MNRAS*, **471**, 2
- Planck Collaboration et al., 2014, *A&A*, **571**, A16
- Pratt G. W., et al., 2010, *A&A*, **511**, A85
- Sasaki T., Matsushita K., Sato K., 2014, *ApJ*, **781**, 36
- Sato K., Matsushita K., Yamasaki N. Y., Sasaki S., Ohashi T., 2014, *Publications of the Astronomical Society of Japan*, **66**
- Simionescu A., et al., 2011, *Science*, **331**, 1576
- Simionescu A., et al., 2013, *ApJ*, **775**, 4
- Simionescu A., Werner N., Mantz A., Allen S. W., Urban O., 2017, *MNRAS*, **469**, 1476
- Springel V., Hernquist L., 2003, *Monthly Notices of the Royal Astronomical Society*, **339**, 312
- Su Y., White Raymond E. I., Miller E. D., 2013, *ApJ*, **775**, 89
- Su Y., Buote D., Gastaldello F., Brighenti F., 2015, *ApJ*, **805**, 104
- Sun M., Voit G. M., Donahue M., Jones C., Forman W., Vikhlinin A., 2009, *The Astrophysical Journal*, **693**, 1142
- Sun M., Sehgal N., Voit G. M., Donahue M., Jones C., Forman W., Vikhlinin A., Sarazin C., 2011, *ApJ*, **727**, L49
- Thölken S., Lovisari L., Reiprich T. H., Hasenbusch J., 2016, *A&A*, **592**, A37
- Urban O., et al., 2014a, *MNRAS*, **437**, 3939
- Urban O., et al., 2014b, *Monthly Notices of the Royal Astronomical Society*, **437**, 3939
- Vazza F., Roncarelli M., Ettori S., Dolag K., 2011, *Monthly Notices of the Royal Astronomical Society*, **413**, 2305
- Vikhlinin A., Kravtsov A., Forman W., Jones C., Markevitch M., Murray S. S., Speybroeck L. V., 2006, *The Astrophysical Journal*, **640**, 691
- Voit G. M., Kay S. T., Bryan G. L., 2005, *MNRAS*, **364**, 909
- Walker S. A., Fabian A. C., Sanders J. S., George M. R., 2012b, *MNRAS*, **424**, 1826
- Walker S. A., Fabian A. C., Sanders J. S., George M. R., 2012a, *Monthly Notices of the Royal Astronomical Society*, **424**, 1826
- Walker S. A., Fabian A. C., Sanders J. S., Simionescu A., Tawara Y., 2013, *MNRAS*, **432**, 554
- Walker S., et al., 2019, *Space Sci. Rev.*, **215**, 7
- Wong K.-W., Irwin J. A., Wik D. R., Sun M., Sarazin C. L., Fujita Y., Reiprich T. H., 2016, *ApJ*, **829**, 49

This paper has been typeset from a $\text{\TeX}/\text{\LaTeX}$ file prepared by the author.